

Superconducting coherence boosted by outer-layer metallic screening in multilayered cuprates

Junhyeok Jeong,¹ Kifu Kurokawa,¹ Shiro Sakai,² Tomotaka Nakayama,³ Kotaro Ando,³ Naoshi Ogane,³ Soonsang Huh,¹ Matthew D. Watson,⁴ Timur K. Kim,⁴ Cephise Cacho,⁴ Chun Lin,⁵ Makoto Hashimoto,⁵ Donghui Lu,⁵ Takami Tohyama,⁶ Kazuyasu Tokiwa,^{3,*} and Takeshi Kondo^{1,7,†}

¹*ISSP, University of Tokyo, Kashiwa, Chiba 277-8581, Japan*

²*Faculty of Science and Technology,
Sophia University, Tokyo 102-8554, Japan*

³*Department of Applied Electronics,
Tokyo University of Science, Tokyo 125-8585, Japan*

⁴*Diamond Light Source Ltd, Harwell Science and
Innovation Campus, Didcot, OX110DE, U.K.*

⁵*Stanford Synchrotron Radiation Lightsource,
SLAC National Accelerator Laboratory,
2575 Sand Hill Road, Menlo Park, CA 94025, U.S.A.*

⁶*Department of Applied Physics, Tokyo University of Science, Tokyo 125-8585, Japan*

⁷*Trans-scale Quantum Science Institute,
The University of Tokyo, Bunkyo-ku, Tokyo 113-0033, Japan*

(Dated: August 1, 2025)

* tokiwa@rs.tus.ac.jp

† kondo1215@issp.u-tokyo.ac.jp

In multilayered high- T_c cuprates with three or more CuO₂ layers per unit cell, the inner CuO₂ planes (IPs) are spatially separated from the dopant layers and thus remain cleaner than the outer planes (OPs). While both interlayer coupling and the presence of clean IPs have been proposed as key factors enhancing superconductivity, their individual roles have been difficult to disentangle, as IPs and OPs typically become superconducting simultaneously. Here we investigate five-layer (Cu,C)Ba₂Ca₄Cu₅O_y (Cu1245) with $T_c = 78$ K and three-layer Ba₂Ca₂Cu₃O_{6(F,O)}₂ (F0223) with $T_c = 100$ K using angle-resolved photoemission spectroscopy (ARPES) for the first time, and uncover an unprecedented situation, in which only the IPs become superconducting while the OPs remain metallic at low temperatures. Model calculations indicate that more than 95% of the OP wavefunction remains confined to OP itself, with minimal hybridization from the superconducting IPs, due to a large energy (or doping) difference between OPs and IPs. In particular, we experimentally realize an ideal configuration: a single superconducting CuO₂ layer sandwiched between heavily overdoped metallic outer layers, which screen disorder originating from the dopant layers. Strikingly, this clean CuO₂ layer exhibits the largest superconducting gap among all known cuprates ($\Delta_0 \sim 60$ meV) and coherent Bogoliubov peaks extending beyond the antiferromagnetic zone boundary—long regarded as the boundary beyond which coherence vanishes in heavily underdoped cuprates. Furthermore, a widely extended coherent flat band emerges at the Brillouin zone edge, overcoming the pseudogap damping effect. Our results introduce a new physical parameter, “the degree of screening,” to investigate the competition between superconductivity and the pseudogap, potentially shedding new light on the longstanding debate regarding its origin—whether a charge density wave (CDW), a pair density wave (PDW), or other mechanisms. The naturally realized, nearly disorder-free superconducting CuO₂ layers offer a model platform for bridging the gap between typically disordered real materials and idealized theoretical models, which generally neglect disorder effects. This will thereby open a new route toward resolving one of the central challenges in condensed matter physics: the microscopic mechanism of high-temperature superconductivity.

I. Introduction

Understanding the microscopic origin of high-temperature superconductivity in cuprates is arguably one of the most central unsolved problems in condensed matter physics. To date, most investigations have concentrated on single- and double-layered cuprates, due to

their structural simplicity and relative ease of crystal growth. However, scanning tunneling microscopy [1, 2] has revealed that CuO₂ layers in these systems are inevitably disordered because of their close proximity to dopant layers, which introduce random potentials. Such disorder effects complicate direct comparison with microscopic theories, which generally assume ideal, disorder-free CuO₂ sheets. Resolving this theory-reality mismatch may bring a breakthrough in formulating a microscopic theory of pairing in high- T_c cuprate research.

This fundamental problem can be overcome by the multilayered cuprates, in which three or more CuO₂ planes stack within a single unit cell. In general notation, the CuO₂ planes in the multilayered system are classified into inner planes (IPs) and outer planes (OPs) with their different doping levels (or local potentials) depending on the relative distance to dopant layers. The OPs directly contact the dopant layers, whereas the IPs do not and are protected by adjacent OPs. The elemental-site sensitive nuclear magnetic resonance (NMR) measurement demonstrates that the IPs are flat and clean, maintaining a homogeneous electronic state, which is unattainable in single- and double-layer compounds [3, 4]. Above all, we should keep in mind that three-layer cuprates, which achieve the highest superconducting (SC) transition temperatures (T_c) among existing materials [5], also host clean IPs; thereby, unveiling the electronic properties of IPs and their relationship with OPs holds the key for elucidating the pairing mechanism in the high- T_c cuprates.

Recently, five- and six-layer cuprates with apical-fluorine structures have been found to exhibit small Fermi pockets in clean inner CuO₂ layers, which is a long-anticipated electronic structure that had eluded experimental realization [6, 7]. Interestingly, while superconductivity occurs in the second inner and outer layers, the innermost layer is reported to remain metallic at the lowest temperatures. However, the SC gap observed in these systems was considerably smaller than that in other cuprates [8–15], leaving open the possibility that the innermost layer hosts proximity-induced superconductivity, which is too weak to detect. In addition, their underdoped outer layer hosts superconductivity with low carrier density, making it highly susceptible to disorder introduced by the directly adjacent dopant layers. Such a disordered OP environment may hinder the penetration of superconducting proximity effects into the inner layers.

A better understanding of multilayer cuprates may be gained by exploring the inverse configuration: The inner, cleaner layer is superconducting, but the outer layers remain metallic at the lowest temperatures. It is particularly intriguing if one could realize a special situation where the IPs open the largest SC gap among all cuprates reported to date, and the OPs are metallic with highly dense carriers. This naturally realized rare heterostructure offers a unique opportunity to distinguish intertwined effects across multiple layers on enhancing T_c in cuprates. Most importantly, this rather unique but simple material setting, where CuO₂ layers are shielded by metallic layers with dense mobile carriers, may be able to fill a

serious gap between real materials and idealized theoretical models, where disorder effects are usually neglected. Moreover, this specific material system may provide insights into artificial heterostructures combining high- T_c cuprates and other compounds, such as topological insulators, with the ultimate goal of realizing topological superconductivity [16–19]. This study, therefore, not only allows investigating the properties of multilayer cuprates but also sheds light on the interlayer physics.

In this article, we report an unprecedented configuration in cuprates, where superconducting CuO₂ planes are sandwiched between highly conductive metallic sheets. These metallic sheets effectively screen out disorder from the dopant layers, allowing us to introduce a new physical parameter—“the degree of screening”—to access the intrinsic electronic properties of cuprates. In particular, we demonstrate that the inner CuO₂ planes in a multilayer high- T_c cuprate host the largest superconducting gap among all known cuprates, while the heavily overdoped metallic outer layers show no superconducting signals or proximity effect. Model calculations reveal that the large energy (or doping) difference between layers blocks interlayer coupling. This prevents superconducting proximity from the inner to the outer planes. Meanwhile, the highly conductive metallic outer layers shield the inner planes from disorder, significantly enhancing superconducting coherence and superfluid density. Consequently, even a single CuO₂ layer can exhibit both a large pairing gap and strong phase stiffness when disorder is removed. We detect a coherent flat band near the zone edge, shedding new light on the origin of the pseudogap—whether it stems from a charge density wave (CDW), a pair density wave (PDW), or other mechanisms. These findings offer a promising route to address the mismatch between real materials and idealized theoretical models that often neglect disorder effects.

II. Results

We begin by presenting the overall electronic structure of Cu1245 with $T_c = 78$ K. In multilayered cuprates, carriers in the CuO₂ planes are distributed from the dopant layers. The doping level, therefore, decreases as the spatial distance from the dopant layers increases [3, 4, 20, 21]. The five-layered Cu1245 (Fig. 1a) consists of three doping-inequivalent CuO₂ planes: outer planes (OP), and two inner planes (IP₁ and IP₀). We observe essentially two Fermi surfaces (FSs), both hole-like and centered at (π, π) (Fig. 1b). According to the above discussion, the larger FS is primarily from the OPs, while the smaller one originates mainly from the IPs. Although a slight band splitting between IP₀ and IP₁ is expected, it is too small to resolve. This may come not only from a limited equipment resolution, but also from unavoidable surface roughness due to the lack of a natural cleavage plane in Cu1245. This causes spectral broadening, hindering the identification of the band separation for IP₀ and IP₁. Thereby, we treat IP₁ and IP₀ together as a single “IP” band. The Fermi momenta k_F

extracted from the FS mapping are plotted in Fig. 1c, with the red and blue circles for IP and OP, respectively. From the FS volume of OP, we estimate a hole carrier concentration of $p(\text{OP}) \sim 28\%$. In contrast, the IP band forms a truncated Fermi arc, within which coherent peaks are particularly sharp and clear.

Figures 1d-h display the ARPES band dispersions from the nodal to the antinodal region. The IP bands marked by red arrows show a band structure typical of cuprates with a d -wave SC gap. While the nodal dispersion crosses E_F with no gap, a SC gap starts opening off the node and gets larger toward the antinode. Near the antinodal region, the Bogoliubov back-bending becomes unclear since coherent peaks are strongly suppressed due to the development of the pseudogap [22, 23]. This makes it difficult to determine the k_F from the gap minimum (dashed line in Fig. 1c).

Strikingly, the OP band (blue arrows) shows very different behavior from the IPs. The band dispersion crosses the E_F along the entire FS. The contrasting results of OPs are more clearly demonstrated in Figs. 2c, d, where the raw EDCs at k_F and those symmetrized across E_F are plotted for the different Fermi angle ϕ (right-bottom inset in Fig. 2e). Interestingly, OP is gapless all along the FS. This is in stark contrast to a d -wave-like gap behavior typical for underdoped cuprates, observed in IP (Figs. 2a, b).

Figure 2e summarizes the gap magnitude for both layers plotted against the d -wave form, $\Delta_0 |\cos(k_x) - \cos(k_y)|/2$, where Δ_0 is the extrapolated gap to the antinode. IP features a clear d -wave superconducting property, having a large $\Delta_0^{\text{IP}} \sim 48$ meV. A deviation from the monotonic d -wave structure near the antinode is a hallmark of the two-gap states due to the presence of the pseudogap typical in underdoped cuprates [10, 22–25]. On the other hand, OP shows no gap, which extends to the antinodal region. Given that the OP layer is heavily overdoped ($p(\text{OP}) \sim 28\%$), and nearly constant peak width at the Fermi energy (E_F) along wide proportions of FS (Figs. 2c, d), this no-gap feature indicates that OPs are in a normal metallic state, without a notable proximity effect induced from IPs. We note here that the current situation differs from $\text{Bi}_2\text{Sr}_2\text{Ca}_2\text{Cu}_3\text{O}_{10+\delta}$ (Bi2223), which exhibits significant interlayer mixing due to Bogoliubov band hybridization [14, 26, 27]: The superconducting OP band causes Bogoliubov back-bending. This results in a band crossing with the IP band, inducing significant interlayer mixing. This is not the case in the current compound since the OP band is in the metallic state at low temperatures.

To quantify the absence of interlayer SC proximity effect, we conduct a tight-binding model calculation for the five-layer structure. We find that two factors are important for the proximity effect: the layer-dependent potential e_l (depending on the distance from the dopant layers) and the interlayer hopping V (Fig. 3g). Although both parameters lead to band separation in energy, their physical roles differ distinctly: V yields interlayer wavefunction mixing, while e_l difference between layers δe suppresses it. A variety of V , e_l

combinations can reproduce a given ARPES data. However, we can estimate the upper bound of V from the data and demonstrate that such a V value is not large enough to open a measurable energy gap in the OP band by the proximity effect from the superconducting IPs (see the Supplementary Information for more details).

To address this, we display in Fig. 3a the ARPES data of the FS and the band dispersions for Cuts 1, 3, and 5 shown in Fig. 1. Calculated results are shown alongside each panel. In both cases in Figs. 3b, c, the SC gap is set to $\Delta_0^{\text{IP}} \sim 48$ meV for IP and zero for OP. Now, we simulate the bands with two specific combinations for parameters V and e_l . In Fig. 3b, we set $V=0$ and choose appropriate e_l for each layer to reproduce the data, as listed in the table of Fig. 3g. The e_l for IP_0 and IP_1 can be particularly guided by the data of Cut 3, which clearly shows a splitting, as demonstrated by extracting the momentum distribution curve (MDC) along the blue arrow in the inset. In this case, the wavefunction mixing is zero simply because the interlayer hopping is set to zero. As expected, the OP spectra show no indication of gap opening (Fig. 3e).

The upper bound of V yielding the interlayer mixing can be found as follows. For this purpose, we focus on the splitting of the IP_1 and IP_0 bands, which is relatively small. Now, we set the potential difference δe between IP_1 and IP_0 to zero, and reproduce their spectral splitting by choosing a value of V (insets of Cut 3 in Fig. 3). We find that a V value which reproduces the data lies between 0.02 and 0.04 eV. Using the larger V (0.04 eV), the calculated band splitting of IPs exceeds the experimental one, as demonstrated in the inset of Fig. 3c, which plots an MDC along the blue arrow. Notably, the calculations show triple bands splitting, which is not observed in the ARPES data. Most importantly, even the overestimated V (0.04 eV) does not open a gap in the OP band (Fig. 3f). This indicates that the SC proximity effect from IPs to the OP band is negligible in the real material.

In Fig. 3h, we estimate the percentage of the wavefunction confinement within OP with respect to V values. We note that the OP has two low-energy eigenstates, since there are two equivalent sheets of the outer layer in the crystal structure (Fig. 1a). As a result, we get two different low-energy states for the k_F points of OP: symmetric (sym.) and antisymmetric (antisym.). Figure 3h displays both results. Even for the upper bound V (0.04 eV), both results show that more than 95% of the spectral weight for the OP band is derived from the OP itself without significant wavefunction mixing from IPs. We note this OP-isolation is mainly due to a large e_l difference between OP and IPs. This suggests that a large energy (or doping) difference between layers suppresses wavefunction mixing, rendering the SC proximity effect negligible in the five-layer Cu1245.

The five-layer Cu1245 enabled us to conclude that the interlayer hopping between the heavily overdoped OP and the underdoped IP can be weak enough to render their interlayer mixing negligible. However, the presence of mutually coupled three IPs (two IP_1 s and one

IP_0) obscures the intrinsic properties of a clean, isolated CuO_2 plane. Moreover, it has been reported that the IPs in Cu1245 are more sensitive to disorder effects than those in other multilayered systems [28]. To avoid these complexities, we now shift our focus to the three-layer F0223. This compound corresponds to $n = 3$ in $\text{Ba}_2\text{Ca}_{n-1}\text{Cu}_n\text{O}_{2n}(\text{F}_y\text{O}_{1-y})_2$. Note that the observation of a small Fermi pocket was achieved in the lightly doped, clean IPs for the five-layer case ($n = 5$) [6]. The three-layer F0223 has the simplest multilayer structure with IPs, in which a single IP is sandwiched between two OPs in the unit cell (Fig. 4a). This compound is therefore ideally suited for the current study. Typically, three-layer cuprates have the highest T_c among series compositions [5]. A widely accepted view to explain the particularly high T_c is that the underdoped IP hosts a large pairing gap but suffers from strong phase fluctuations, whereas the overdoped OP compensates for this by providing phase stiffness [29–31]. Although intriguing, and supported by experiment [14, 26, 27], this scenario premises a hybridization between OP and IP [30, 31]. An intriguing question is what happens if this interlayer hybridization is negligibly small, and the IP essentially remains isolated in the three-layer structure; this will be addressed below.

Figure 4b presents the FS mapping of pristine F0223 with $T_c = 100$ K, showing two spectral branches of IP and OP, which lie close to each other but are clearly separated. We find that both IP and OP open the SC gap (Fig. 4e-h, and 4m), similar to those in optimally doped Bi2223: $\Delta_0^{\text{IP}} \sim 60$ meV, and $\Delta_0^{\text{OP}} \sim 35$ meV [14, 32]. Yet, a clear difference is observed: Not only the IP band but also the OP band shows a two-gap behavior, deviating from the monotonic d -wave symmetry (Fig. 4m). The spectra with a larger energy scale exhibit a broad lineshape indicative of the pseudogap near the antinode (Figs. 4g, green arrows). This indicates that both IP and OP bands are located in the underdoped regime, being consistent with the lower $T_c = 100$ K of the current sample than $T_c \sim 120$ K for optimally doped F0223 [3, 33].

For both IP and OP, the FSs show arc-like features: Coherent, sharp peaks are observed only in the limited region near the node, and broad spectra characteristic of a pseudogap are observed outside that arc region [22, 23, 34]. This makes it difficult to estimate doping levels accurately from the FS areas. The momentum splitting between IP and OP is resolvable, yet is notably smaller than that in optimally doped Bi2223 [14, 32]. This indicates that the doping-level difference between IP and OP in the present F0223 sample is smaller than that of optimally doped Bi2223. Arguments in Fig. 3 further suggest that the interlayer coupling likely exceeds that in optimally doped Bi2223.

To suppress the interlayer coupling (or band hybridization) and reproduce the situation of an isolated clean IP, we perform surface doping on F0223 and enhance the doping level difference between the IP and OP. The widely used technique for surface doping employs alkali-metal deposition [7, 35, 36], which, however, decreases hole-doping toward the under-

doped regime. For hole-doping in cuprates, *in-situ* ozone annealing has been demonstrated to be effective [9, 37]. In this study, instead, we used a rather simple yet robust method: exposing the cleaved surface to a small air leak ($\sim 3 \times 10^{-9}$ Torr) in the measurement vacuum chamber. This method effectively increases the doping level toward the overdoped side, as previously demonstrated [38].

Unlike the pristine sample, the FS mapping of the surface-doped sample reveals a clearer separation between the IP and OP (Fig. 4c). In Fig. 4d, we extract momentum distribution curves (MDCs) along the nodal cuts indicated in Figs. 4b, c and fit them with Voigt functions to quantify the k_F splitting [39]. After surface doping, the separation between the IP and OP increases by more than a factor of two. Interestingly, however, the IP peak positions remain nearly unchanged, indicating that only the OP is significantly doped. This is further supported by full extraction of k_F points along the FS within the red box shown in Figs. 4b, c (inset of Fig. 4m). The OP band shifts significantly to the overdoped region. This lifts the saddle point at $(\pi, 0)$ above E_F , causing the Lifshitz transition from the original hole-like topology centered at (π, π) to an electron-like topology centered at $(0, 0)$ [11, 37, 40]. Consequently, the doping level (p) estimated from the FS area is drastically increased from the underdoped regime ($p(\text{OP}) \sim 8\%$) to the heavily overdoped regime ($p(\text{OP}) \sim 30\%$), which typically lies outside the superconducting T_c dome [41]. In contrast, the IP band remains nearly unchanged between the pristine and surface-doped samples. A small amount of carrier doping in the IPs may still occur, though the estimated amount is less than 1%, as determined from the errors in the k_F position. The discrepancy in doping between OPs and IPs can be naturally explained by their multilayered structure. The surface doping primarily influences the dopant layer (cleavage plane [42]); consequently, only the OPs adjacent to it are effectively doped.

We find that the layer-selective doping also alters the layer dependence of the SC gap. Figures 4i-l plot the raw and symmetrized EDCs for OP and IP at various k_F points of surface-doped sample. Notably, the OP gap becomes entirely closed (Fig. 4j). This indicates that the OP becomes a heavily overdoped normal metallic state, similarly to the OPs of the five-layer Cu1245. By contrast, the IP gap remains robust and nearly identical between the pristine and surface-doped samples (Figs. 4h, l). Figure 4m presents the extracted SC gap magnitude as a function of the d -wave form. The extrapolated IP gap to antinode (Δ_0^{IP}) reaches ~ 60 meV, which is comparable to the IP gaps of other three-layered cuprates such as Bi2223 and $\text{HgBa}_2\text{Ca}_2\text{Cu}_3\text{O}_{8+\delta}$ (Hg1223), which has the highest T_c in cuprates ($T_c = 130$ K) [14, 27, 32, 43]. In stark contrast, the energy gap in OP, which is $\Delta_0^{\text{OP}} \sim 35$ meV in the pristine sample, vanishes in the doped sample. Notably, both the gap magnitude and the FS topology remain unchanged in IP, indicating that surface doping has little effect on the doping level of the IP.

Importantly, despite minimized doping variation in the IP, the SC coherence peaks in the IP band become significantly sharper in the surface-doped sample (Figs. 4g, k). In contrast, the spectrum of OP becomes significantly broadened, even though it is in a heavily overdoped condition. This indicates that the sample surface is damaged during the surface doping process; however, it also demonstrates that the IP is protected from the OP, and the sharpening of the IP spectra should be intrinsic. Notably, the MDC peaks of the pristine sample are sharper than those of the surface-doped sample (Fig. 4d). The surface degradation may have reduced the spectral quality of the IP, to some extent, in the surface-doped sample. Considering such adverse conditions, this intrinsic sharpening is particularly striking. In the heavily underdoped cuprates, it is established that the coherent peaks, observed around the nodal region, vanish across the antiferromagnetic zone boundary (AFZB) toward the antinode. This has been revealed by both ARPES [8, 10, 22, 23, 25, 44] and scanning tunneling microscopy (STM) measurements [45]. Notably, this behavior is also observed in the band of the underdoped inner CuO₂ plane in the optimally doped three-layered cuprates [27, 43], including Hg1223 with the highest T_c in cuprates ($T_c=130$ K) [43]. This feature is also confirmed in the underdoped IP band of the current pristine sample (colored arrows in Fig. 4g). Intriguingly, however, the surface-doped IP exhibits coherent, sharp peaks in the same momentum region (colored arrows in Fig. 4l). The enlarged Bogoliubov band (or an extended portion of the Fermi surface that contributes to superconductivity) implies a substantial increase in superfluid density; thus, the SC phase stiffness is strengthened. Thus, a large pairing gap ($\Delta_0^{\text{IP}} \sim 60$ meV, the largest in cuprates) and strong phase stiffness are simultaneously realized in the single CuO₂ sheet. It is known that even a single-layer cuprate can reach a high T_c of ~ 100 K, as exemplified in HgBa₂CuO_{4+δ} (Hg1201) [46]. Notably, Δ_0 of Hg1201 is only ~ 40 meV [15], which is 1.5 times smaller than that of the IP of F0223 ($\Delta_0^{\text{IP}} \sim 60$ meV). Although the T_c of the surface-doped state is not determined, it opens possibility that the system with a single clean IP shielded by metallic layers with dense carriers may be capable of reaching a T_c well above 100 K. Note that more heavily doped samples of F0223 indeed show $T_c \sim 120$ K [3, 33]. Although they are polycrystalline, they may be in a condition similar to that of our surface-doped state. The synthesis of a single crystal with such a higher doping level has not yet been achieved; if successful, it would allow both T_c and ARPES measurements, offering a compelling direction for future research.

The simplest setting of a single CuO₂ layer per unit cell without disorder will provide a model case to compare the microscopic theory for the pairing mechanism, which does not include the disorder effect. We further find a rather drastic change in the IP band, particularly near the antinode, due to the SC coherence enhancement. Figures 5b-f compare the energy-momentum dispersions for both the pristine and surface-doped crystals, taken

along the momentum cuts labeled as Cuts 1 to 5 (orange lines in Fig. 5a). In the pristine sample, as one moves from Cut 1 toward Cut 5 (approaching the antinode), both the IP and OP bands become blurred and weak in intensity, reflecting the pseudogap-induced spectral damping characteristic of underdoped cuprates.

In contrast, the IP band in the surface-doped sample remains sharp and well-defined even at the antinode (Cut 5). Meanwhile, the OP band shifts above E_F around $(\pi, 0)$, consistent with a Lifshitz transition into the heavily overdoped regime [11, 37, 40]. Interestingly, the band dispersion of the coherent peak is much shallower than that before doping (for example, compare panels for Cut 3 in Fig. 5d). This indicates that the coherent peak dispersion is highly renormalized. To quantify the surface doping effect on the IP band, we integrated the EDCs over a defined momentum window (marked by grey lines in Fig. 5f) for both samples and compared them in Fig. 5g. In the pristine sample, only a hump-like feature is observed around -65 meV in the IP band. In the surface-doped sample, a sharp peak with almost the same width as that of the SC coherent peak near the node emerges at the same energy position as the hump in the pristine sample. Remarkably, the coherent peaks show a very flat band near the Brillouin zone edge. This is clearly observed along the momentum cut on the zone boundary (Fig. 5f).

We found that the coherent flat band is extended two-dimensionally in a wide momentum range around $(\pi, 0)$. Figure 5h shows the FS mapping of the surface-doped F0223. We select four particular momentum cuts (Cuts A to D, indicated by white lines) centered at $(\pi, 0)$ and extract the energy-momentum dispersions in Figs. 5i-l. These clearly show coherent peaks and isotropic flatness; the coherent flat band of IP two-dimensionally extends over a wide momentum space around $(\pi, 0)$. This illustrates that SC coherent electrons at $(\pi, 0)$ are spatially localized. Importantly, such a flat band is absent in the pristine sample, where the IP spectra contain only a broad hump reflecting the pseudogap state, a typical feature of deeply underdoped cuprates [8, 10, 22, 23, 25, 44]. These findings suggest that spatially localized coherent electrons emerge only when disorder is effectively screened from the dopant layer—specifically, by locating the CuO_2 plane between metallic layers with dense mobile carriers—thereby mitigating the pseudogap-induced spectral damping. These results may indicate a competition between electron coherence and the incoherent density wave, such as CDW [34, 47–51] and PDW [52–54], and its sensitivity to the disorder induced by the dopant layer. Previous studies have revealed competition through variations of the doping level in the CuO_2 layer [8, 55]. Our results offer a new approach to investigating competition by tuning the screening of the CuO_2 layer, rather than varying the doping level. Most importantly, this approach may realize an ideal system that can be directly compared with an idealized theory, excluding the disorder effect. This provides a promising avenue for identifying the origin of the pseudogap—a key issue in understanding the microscopic

physics of underdoped cuprates.

III. Conclusion and discussion

In conclusion, we have experimentally realized an unprecedented situation in cuprates: single CuO₂ layers exhibiting the largest SC gap observed to date, sandwiched between metallic sheets with dense mobile carriers that effectively screen disorder originating from the dopant layers. Notably, no SC proximity effect was detected in the metallic layers. The strategy behind our results is an interlayer *decoupling*, achieved through excess doping of the outer layers. The resulting large doping-level (or potential) difference between layers prevents orbital hybridization, thereby decoupling the superconducting inner layers from disorder from the dopant layers, either directly or via the outer CuO₂ planes. This system uniquely offers an experimentally accessible, nearly ideal platform for directly validating long-standing microscopic theories of pairing, previously hindered by disorder. According to our model calculations, the proximity-induced wavefunction mixing effect is minimal due to the large doping (or potential) level difference between the layers. As a result, the wavefunctions remain localized within each CuO₂ layer. Intriguingly, we found that the existence of heavily overdoped metallic OP significantly enhances the SC coherence in IP, overcoming the damping effect of the pseudogap states. This points to a simultaneous realization of strong pairing and strong phase stiffness in single CuO₂ layers. Estimating the T_c of the surface-doped state—or the T_c of single crystals under a similar condition, if successfully synthesized—will be a key future step to further validate and strengthen the present conclusions.

Coherent flat bands around the Brillouin zone edge demonstrate that the spatially localized coherent electrons with a specific momentum $(\pi, 0)$ emerge in the screened, clean CuO₂ plane. These findings may indicate the partial development of strongly bound coherent pairs among $(\pi, 0)$ electrons, competing with the pseudogap state. The results demonstrate that the purity of IPs can be tuned by the metallic conductivity of OPs, introducing the degree of screening as a new physical parameter in cuprate research. This new research direction may help resolve the reality-theory mismatch, which has been one of the major obstacles to constructing microscopic pairing mechanisms in high- T_c cuprates.

Our results provide several further implications. In the study of artificial heterostructures, superconductors—including cuprates—are often used as a substrate source to induce SC proximity effects [19, 56]. The present results illustrate that not only the SC coherence length, as frequently argued, but also the degree of orbital hybridization between the superconductor and other materials (such as topological insulators) is crucial [57]. Our findings also suggest an explanation for why Y-Ba-Cu-O compounds are relatively clean systems among double-layered cuprates, as revealed by the sharp peak in NMR spectra [4]. This is

mainly because the CuO₂ layers are sandwiched by metallic CuO chains [58, 59], which can effectively screen disorder effects.

We also point out that the SC gap in Y-Ba-Cu-O emerges in the chains only at specific momentum points where the two-dimensional FS of the CuO₂ layers intersects with the one-dimensional FS of the CuO chains [60]. This occurs precisely because the electrostatic potentials of the CuO₂ layers and CuO chains align, allowing the hybridization between them. As a result, the proximity effect from the CuO₂ layers to the chains is activated, leading to the emergence of a SC gap at the momentum region where the hybridized bands intersect. Our results will open a new avenue for designing disorder-resilient, high- T_c materials based on engineered electronic screening and hybridization control.

IV. Methods

The single crystals of the five-layer compound Cu1245 ($T_c = 78$ K) and the three-layer F0223 ($T_c = 100$ K) were grown by a high-pressure method, as described elsewhere [61]. The T_c was determined by the onset of SC diamagnetism using a dc SQUID magnetometer. ARPES experiments were carried out at the beamline I05 of Diamond Light Source and the beamline BL5-2 of Stanford Synchrotron Radiation Lightsource. Cu1245 and pristine F0223 were *in-situ* cleaved and measured under vacuum better than 8×10^{-11} Torr. Surface doping of F0223 was achieved by exposing the cleaved crystal surface to the air leak of $\sim 3 \times 10^{-9}$ Torr in the ARPES measurement chamber [38]. Measurements were performed using a photon energy of $h\nu = 55$ eV at a temperature of $T \sim 7$ K. The total energy resolution was set to ~ 12 meV.

- [1] Pan, S. H. *et al.* Microscopic electronic inhomogeneity in the high- T_c superconductor Bi₂Sr₂CaCu₂O_{8+x}. *Nature* **413**, 282–285 (2001).
- [2] McElroy, K. *et al.* Atomic-scale sources and mechanism of nanoscale electronic disorder in Bi₂Sr₂CaCu₂O_{8+δ}. *Science* **309**, 1048–1052 (2005).
- [3] Shimizu, S. *et al.* High-temperature superconductivity and antiferromagnetism in multilayer cuprates: ⁶³Cu and ¹⁹F NMR on five-layer Ba₂Ca₄Cu₅O₁₀(F,O)₂. *Phys. Rev. B* **85**, 1–12 (2012).
- [4] Mukuda, H., Shimizu, S., Iyo, A. & Kitaoka, Y. High- T_c Superconductivity and Antiferromagnetism in Multilayered Copper Oxides –A New Paradigm of Superconducting Mechanism–. *J. Phys. Soc. Jpn.* **81**, 011008 (2012).

- [5] Iyo, A. *et al.* T_c vs n relationship for multilayered high- T_c superconductors. *J. Phys. Soc. Jpn.* **76**, 094711 (2007).
- [6] Kunisada, S. *et al.* Observation of small Fermi pockets protected by clean CuO₂ sheets of a high- T_c superconductor. *Science* **838**, 833–838 (2020).
- [7] Kurokawa, K. *et al.* Unveiling phase diagram of the lightly doped high- T_c cuprate superconductors with disorder removed. *Nat. Commun.* **14**, 4064 (2023).
- [8] Kondo, T., Khasanov, R., Takeuchi, T., Schmalian, J. & Kaminski, A. Competition between the pseudogap and superconductivity in the high- T_c copper oxides. *Nature* **457**, 296–300 (2009).
- [9] Zhong, Y. G. *et al.* Continuous doping of a cuprate surface: Insights from in situ angle-resolved photoemission. *Phys. Rev. B* **98** (2018).
- [10] Vishik, I. *et al.* Phase competition in trisection superconducting dome. *Proc. Natl. Acad. Sci. U.S.A.* **109**, 18332–18337 (2012).
- [11] Zhong, Y. *et al.* Differentiated roles of Lifshitz transition on thermodynamics and superconductivity in La_{2-x}Sr_xCuO₄. *Proc. Natl. Acad. Sci. U.S.A.* **119**, e2204630119 (2022).
- [12] Nakayama, K. *et al.* Bulk and surface low-energy excitations in YBa₂Cu₃O_{7-δ} studied by high-resolution angle-resolved photoemission spectroscopy. *Phys. Rev. B* **75**, 014513 (2007).
- [13] Ideta, S. *et al.* Energy scale directly related to superconductivity in high- T_c cuprates: Universality from the temperature-dependent angle-resolved photoemission of Bi₂Sr₂Ca₂Cu₃O_{10+δ}. *Phys. Rev. B* **85** (2012).
- [14] Kunisada, S. *et al.* Observation of Bogoliubov Band Hybridization in the Optimally Doped Trilayer Bi₂Sr₂Ca₂Cu₃O_{10+δ}. *Phys. Rev. Lett.* **119**, 217001 (2017).
- [15] Vishik, I. M. *et al.* Angle-resolved photoemission spectroscopy study of HgBa₂CuO_{4+δ}. *Phys. Rev. B* **89**, 195141 (2014).
- [16] Veldhorst, M. *et al.* Josephson supercurrent through a topological insulator surface state. *Nat. Mater.* **11**, 417–421 (2012).
- [17] Yang, F. *et al.* Proximity-effect-induced superconducting phase in the topological insulator Bi₂Se₃. *Phys. Rev. B* **86**, 134504 (2012).
- [18] Zareapour, P. *et al.* Proximity-induced high-temperature superconductivity in the topological insulators Bi₂Se₃ and Bi₂Te₃. *Nat. Commun.* **3**, 1056 (2012).
- [19] Wang, E. *et al.* Fully gapped topological surface states in Bi₂Se₃ films induced by a *d*-wave high-temperature superconductor. *Nat. Phys.* **9**, 621–625 (2013).
- [20] Kotegawa, H. *et al.* NMR study of carrier distribution and superconductivity in multilayered high- T_c cuprates. *J. Phys. Chem. Solids* **62**, 171–175 (2001).
- [21] Mori, M., Tohyama, T. & Maekawa, S. Electronic states and superconductivity in multilayer

- high- T_c cuprates. *Phys. Rev. B* **66**, 064502 (2002).
- [22] Tanaka, K. *et al.* Distinct Fermi-momentum-dependent energy gaps in deeply underdoped Bi2212. *Science* **314**, 1910–1913 (2006).
- [23] Kondo, T., Takeuchi, T., Kaminski, A., Tsuda, S. & Shin, S. Evidence for Two Energy Scales in the Superconducting State of Optimally Doped $(\text{Bi}, \text{Pb})_2(\text{Sr}, \text{La})_2\text{CuO}_{6+\delta}$. *Phys. Rev. Lett.* **98**, 267004 (2007).
- [24] Lee, W.-S. *et al.* Abrupt onset of a second energy gap at the superconducting transition of underdoped Bi2212. *Nature* **450**, 81–84 (2007).
- [25] Yoshida, T. *et al.* Universal versus Material-Dependent Two-Gap Behaviors of the High- T_c Cuprate Superconductors: Angle-Resolved Photoemission Study of $\text{La}_{2-x}\text{Sr}_x\text{CuO}_4$. *Phys. Rev. Lett.* **103**, 037004 (2009).
- [26] Ideta, S. *et al.* Hybridization of Bogoliubov Quasiparticles between adjacent CuO 2 layers in the triple-layer cuprate $\text{Bi}_2\text{Sr}_2\text{Ca}_2\text{Cu}_3\text{O}_{10+\delta}$ studied by angle-resolved photoemission spectroscopy. *Phys. Rev. Lett.* **127**, 217004 (2021).
- [27] Luo, X. *et al.* Electronic origin of high superconducting critical temperature in trilayer cuprates. *Nat. Phys.* **19**, 1841–1847 (2023).
- [28] Mukuda, H. *et al.* Disorder-driven quantum phase transition from antiferromagnetic metal to insulating state in multilayered high- T_c cuprate $(\text{Cu}, \text{C})\text{Ba}_2\text{Ca}_4\text{Cu}_5\text{O}_y$. *J. Phys. Soc. Jpn.* **75**, 123702–123702 (2006).
- [29] Kivelson, S. A. Making high T_c higher: a theoretical proposal. *Physica B: Condensed Matter* **318**, 61–67 (2002).
- [30] Berg, E., Orgad, D. & Kivelson, S. A. Route to high-temperature superconductivity in composite systems. *Phys. Rev. B* **78**, 094509 (2008).
- [31] Okamoto, S. & Maier, T. A. Enhanced superconductivity in superlattices of high- T_c cuprates. *Phys. Rev. Lett.* **101**, 156401 (2008).
- [32] Ideta, S. *et al.* Enhanced superconducting gaps in the trilayer high-temperature $\text{Bi}_2\text{Sr}_2\text{Ca}_2\text{Cu}_3\text{O}_{10+\delta}$ cuprate superconductor. *Phys. Rev. Lett.* **104**, 1–4 (2010).
- [33] Shimizu, S. *et al.* Antiferromagnetism, superconductivity, and pseudogap in three-layered high- T_c cuprates $\text{Ba}_2\text{Ca}_2\text{Cu}_3\text{O}_6(\text{F}, \text{O})_2$ probed by Cu-NMR. *Phys. Rev. B* **83**, 214514 (2011).
- [34] Shen, K. M. *et al.* Nodal quasiparticles and antinodal charge ordering in $\text{Ca}_{2-x}\text{Na}_x\text{CuO}_2\text{Cl}_2$. *Science* **307**, 901–904 (2005).
- [35] Fournier, D. *et al.* Loss of nodal quasiparticle integrity in underdoped $\text{YBa}_2\text{Cu}_3\text{O}_{6+x}$. *Nat. Phys.* **6**, 905–911 (2010).
- [36] Hu, C. *et al.* Momentum-resolved visualization of electronic evolution in doping a mott insulator. *Nat. Commun.* 1–10 (2021).

- [37] Drozdov, I. K. *et al.* Phase diagram of $\text{Bi}_2\text{Sr}_2\text{CaCu}_2\text{O}_{8+\delta}$ revisited. *Nat. Commun.* **9**, 5210 (2018).
- [38] Palczewski, A. D. *et al.* Controlling the carrier concentration of the high-temperature superconductor $\text{Bi}_2\text{Sr}_2\text{CaCu}_2\text{O}_{8+\delta}$ in angle-resolved photoemission spectroscopy experiments. *Phys. Rev. B* **81**, 104521 (2010).
- [39] Smit, S. *et al.* Momentum-dependent scaling exponents of nodal self-energies measured in strange metal cuprates and modelled using semi-holography. *Nat. Commun.* **15**, 4581 (2024).
- [40] Kondo, T. *et al.* Hole-concentration dependence of band structure in $(\text{Bi}, \text{Pb})_2(\text{Sr}, \text{La})_2\text{CuO}_{6+\delta}$ determined by the angle-resolved photoemission spectroscopy. *J. Electron Spectrosc. Relat. Phenom.* **137**, 663–668 (2004).
- [41] Keimer, B., Kivelson, S. A., Norman, M. R., Uchida, S. & Zaanen, J. From quantum matter to high-temperature superconductivity in copper oxides. *Nature* **518**, 179–186 (2014).
- [42] Sugimoto, A. *et al.* Multilayered cuprate superconductor $\text{Ba}_2\text{Ca}_5\text{Cu}_6\text{O}_{12}(\text{O}_{1-x}, \text{F}_x)_2$ studied by temperature-dependent scanning tunneling microscopy and spectroscopy. *Phys. Rev. B* **95**, 174508 (2017).
- [43] Horio, M. *et al.* Enhanced Superconducting Gap in the Outer CuO_2 Plane of the Trilayer Cuprate $(\text{Hg}, \text{Re})\text{Ba}_2\text{Ca}_2\text{Cu}_3\text{O}_{8+\delta}$. *Phys. Rev. Lett.* **135**, 046501 (2025).
- [44] Chatterjee, U. *et al.* Observation of a d -wave nodal liquid in highly underdoped $\text{Bi}_2\text{Sr}_2\text{CaCu}_2\text{O}_{8+\delta}$. *Nat. Phys.* **6**, 99–103 (2010).
- [45] Kohsaka, Y. *et al.* How Cooper pairs vanish approaching the Mott insulator in $\text{Bi}_2\text{Sr}_2\text{CaCu}_2\text{O}_{8+\delta}$. *Nature* **454**, 1072–1078 (2008).
- [46] Barišić, N. *et al.* Demonstrating the model nature of the high-temperature superconductor $\text{HgBa}_2\text{CuO}_{4+\delta}$. *Phys. Rev. B* **78**, 054518 (2008).
- [47] Hoffman, J. *et al.* Imaging quasiparticle interference in $\text{Bi}_2\text{Sr}_2\text{CaCu}_2\text{O}_{8+\delta}$. *Science* **297**, 1148–1151 (2002).
- [48] Vershinin, M. *et al.* Local ordering in the pseudogap state of the high- T_c superconductor $\text{Bi}_2\text{Sr}_2\text{CaCu}_2\text{O}_{8+\delta}$. *Science* **303**, 1995–1998 (2004).
- [49] Wise, W. D. *et al.* Imaging nanoscale Fermi-surface variations in an inhomogeneous superconductor. *Nat. Phys.* **5**, 213–216 (2009).
- [50] da Silva Neto, E. H. *et al.* Ubiquitous interplay between charge ordering and high-temperature superconductivity in cuprates. *Science* **343**, 393–396 (2014).
- [51] Chang, J. *et al.* Direct observation of competition between superconductivity and charge density wave order in $\text{YBa}_2\text{Cu}_3\text{O}_{6.67}$. *Nat. Phys.* **8**, 871–876 (2012).
- [52] Edkins, S. D. *et al.* Magnetic field-induced pair density wave state in the cuprate vortex halo. *Science* **364**, 976–980 (2019).

- [53] Hamidian, M. *et al.* Detection of a Cooper-pair density wave in $\text{Bi}_2\text{Sr}_2\text{CaCu}_2\text{O}_{8+x}$. *Nature* **532**, 343–347 (2016).
- [54] Du, Z. *et al.* Imaging the energy gap modulations of the cuprate pair-density-wave state. *Nature* **580**, 65–70 (2020).
- [55] Hashimoto, M. *et al.* Direct spectroscopic evidence for phase competition between the pseudogap and superconductivity in $\text{Bi}_2\text{Sr}_2\text{CaCu}_2\text{O}_{8+\delta}$. *Nat. Mater.* **14**, 37–42 (2015).
- [56] Perconte, D. *et al.* Tunable Klein-like tunnelling of high-temperature superconducting pairs into graphene. *Nat. Phys.* **14**, 25–29 (2018).
- [57] Yilmaz, T. *et al.* Absence of a proximity effect for a thin-films of a Bi_2Se_3 topological insulator grown on top of a $\text{Bi}_2\text{Sr}_2\text{CaCu}_2\text{O}_{8+\delta}$ cuprate superconductor. *Phys. Rev. Lett.* **113**, 067003 (2014).
- [58] Hussey, N. E., Nozawa, K., Takagi, H., Adachi, S. & Tanabe, K. Anisotropic resistivity of $\text{YBa}_2\text{Cu}_4\text{O}_8$: Incoherent-to-metallic crossover in the out-of-plane transport. *Phys. Rev. B* **56**, R11423 (1997).
- [59] Lee, Y.-S., Segawa, K., Ando, Y. & Basov, D. Coherence and Superconductivity in Coupled One-Dimensional Chains: A Case Study of $\text{YBa}_2\text{Cu}_3\text{O}_y$. *Phys. Rev. Lett.* **94**, 137004 (2005).
- [60] Kondo, T. *et al.* Anomalies in the Fermi Surface and Band Dispersion of Quasi-One-Dimensional CuO Chains in the High-Temperature Superconductor $\text{YBa}_2\text{Cu}_4\text{O}_8$. *Phys. Rev. Lett.* **105**, 267003 (2010).
- [61] Watanabe, T. *et al.* Synthesis and Physical Properties of $(\text{Cu},\text{M})\text{Ba}_2\text{Ca}_3\text{Cu}_4\text{O}_z$ ($\text{M}=\text{C,Mg,Ni,Al,Zn,Tl}$). *J. Low Temp. Phys.* **117**, 753–757 (1999).

Acknowledgements

We thank Y. Tanaka for insightful discussions, T. Yamauchi and Y. Kohama for help with the magnetic susceptibility measurements. We thank Diamond Light Source for access to beamline I05 under proposals SI36822, SI30646, SI28930, SI25416, and Stanford Synchrotron Radiation Lightsource for access to beamline BL5-2 under proposal S-XV-ST-6368A that contributed to the results presented here. This work was supported by the JSPS KAKENHI (Grant Numbers: JP21H04439, JP23K17351, JP25H01250, and JP25H01246), the Asahi Glass Foundation, MEXT Q-LEAP (Grant No. JPMXS0118068681), The Murata Science Foundation, The Mitsubishi Foundation, and Toray Science Foundation.

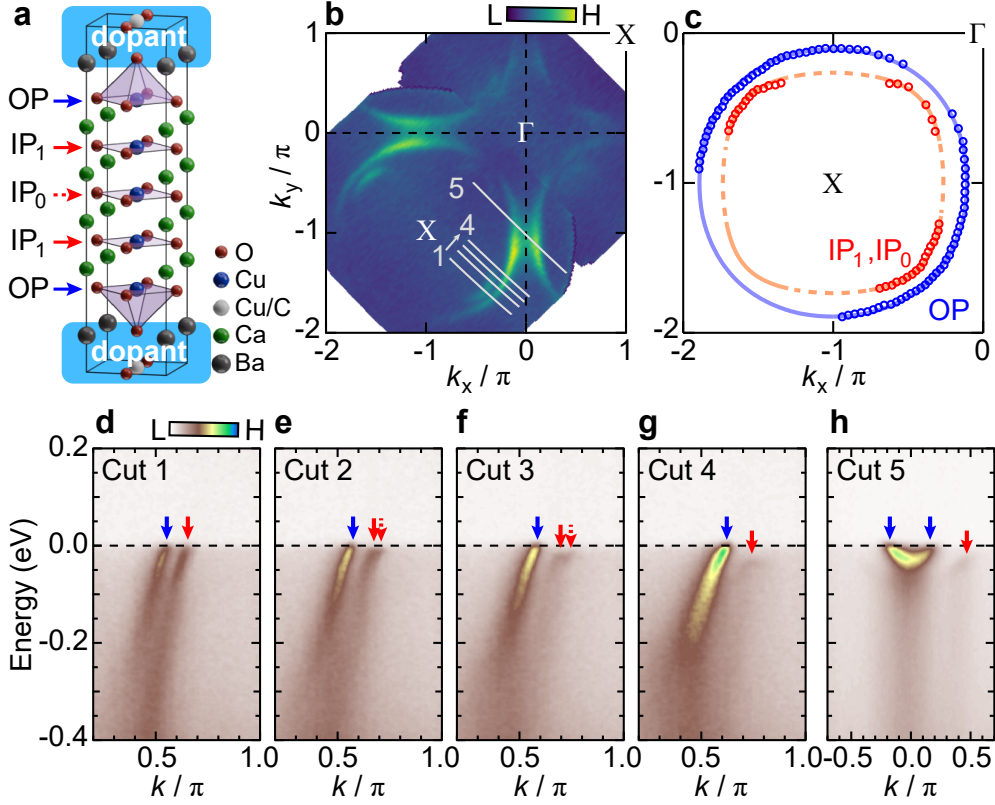


FIG. 1. Fermi surface and band dispersions of the five-layer Cu1245. **a**, Crystal structure of Cu1245. **b**, Fermi surface (FS) of Cu1245 measured by ARPES. Grey lines indicate the momentum cuts used to show the dispersions in **(d-h)**. **c**, Fermi surface determined by the FS map in **(b)**. Red and blue circles indicate the Fermi momentum (k_F) points of IP and OP, respectively. Colored lines are the tight-binding fit to the data. **d-h**, ARPES band dispersions along momentum cuts indicated in **(b)**. Blue and red arrows mark the location of k_F for the OP and IP bands. In Cuts 2 and 3, two bands from IPs are observed.

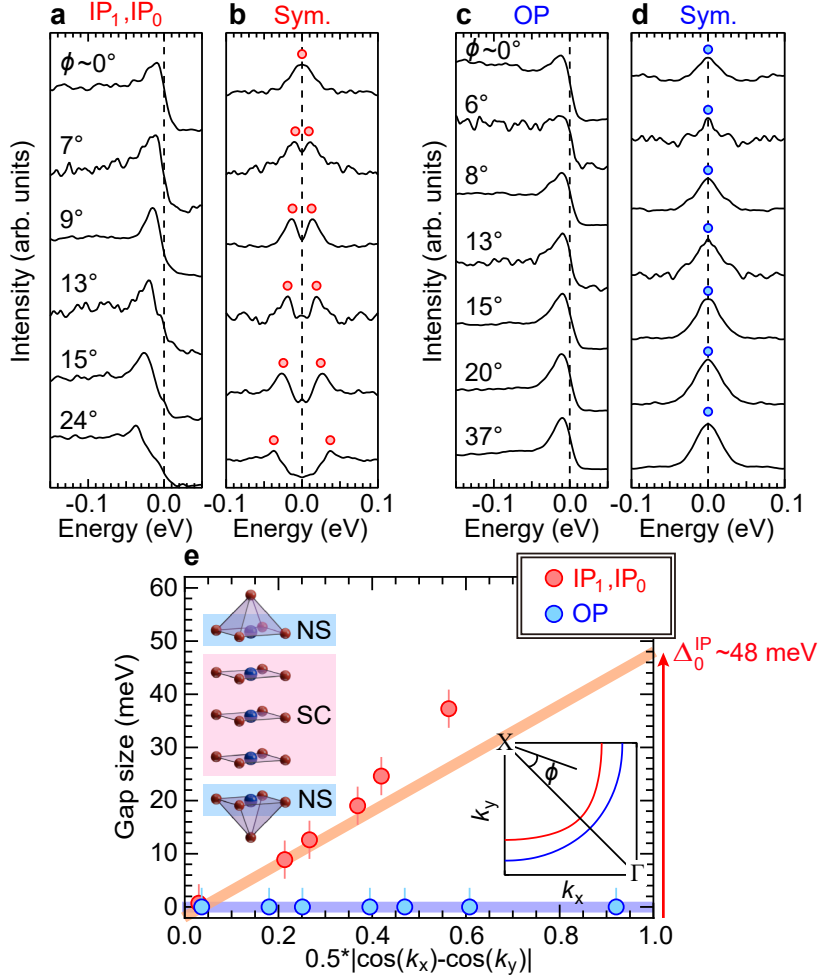


FIG. 2. Superconducting gaps in the five-layer Cu1245 **a**, EDCs of IP taken at various k_F points. ϕ is the angle from the node, as indicated in the right-bottom inset of **(e)**. **b**, Symmetrized EDCs of **(a)**. Colored circles indicate SC coherent peak positions. **c**, **d**, Similar measurement as **(a, b)**, respectively, but for the OP band. **e**, Summary of the SC gap sizes of Cu1245, plotted as a function of d -wave. The top-left inset summarizes our results for the Cu1245 sample: IP is under SC state, while OP is under normal state (NS).

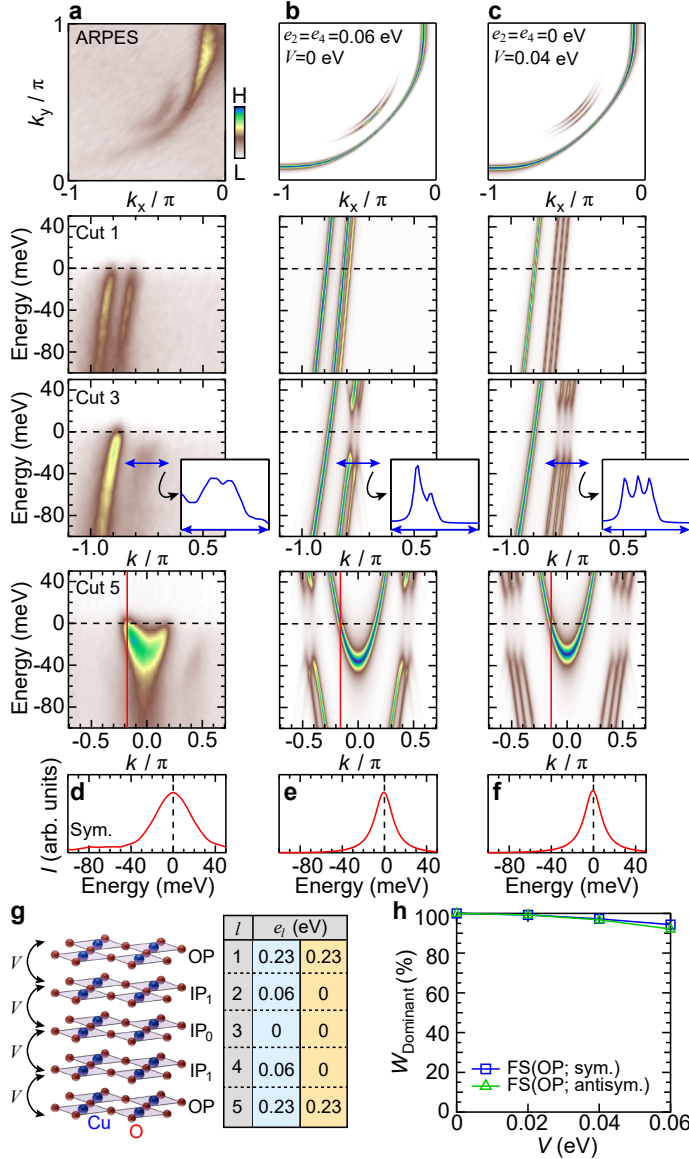


FIG. 3. Model calculations for the five-layer Cu1245 **a**, Enlarged plots of ARPES data of Cu1245 shown in Fig. 1. The first row corresponds to FS mapping. The second, third, and fourth row correspond to Cut 1, 3, and 5 of Fig. 1(d), (f), and (h), respectively. The inset of Cut3 shows a MDC curve along the blue arrow. **b**, Model calculations based on (a), by setting IP₁ potential $e_2 = e_4 = 0.06$ eV, and zero interlayer hopping $V = 0$ eV. **c**, Similar model calculations with (b), but setting zero IP₁ potential $e_2 = e_4 = 0$ eV, and interlayer hopping $V = 0.04$ eV. For Cut 3 of (a-c), MDC along a blue arrow is extracted in the inset. **d**, Symmetrized EDC taken at k_F from the OP band in Cut 5. This is the same curve shown in Fig. 2d (37°). **e**, **f**, Similar to (d), but for the model calculations of (b, c). **g**, Schematic illustration for the model calculation. V and e_l are the interlayer hopping and layer-dependent electronic potential, respectively. Right table shows e_l values set to obtain (b, c). **h**, The weight of the OP wavefunction contribution to the FS of OP itself. Since there are two equivalent OPs in the five-layer system, we obtain two different low-energy states for the FS. (sym. and antisym.). e_l are set to the same in (c).

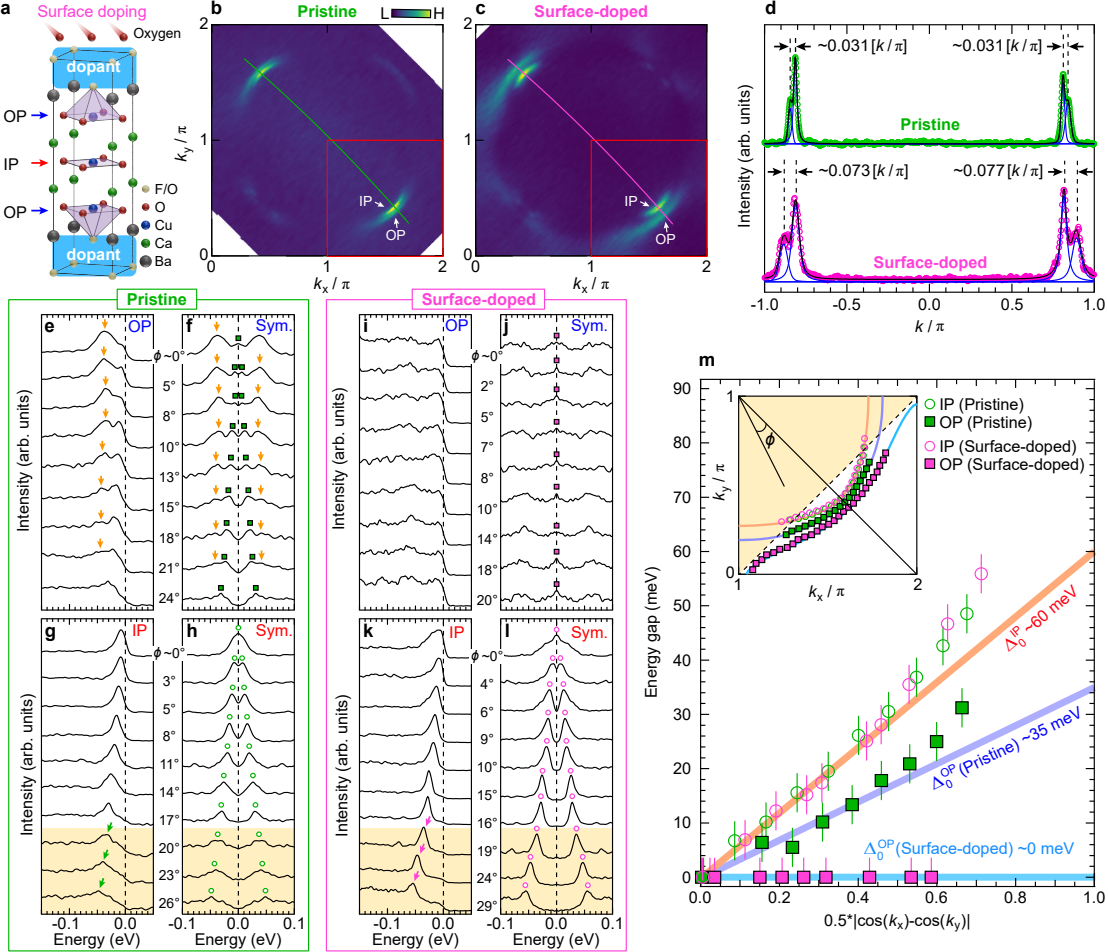


FIG. 4. Fermi surface mapping and superconducting gap in the pristine and surface-doped three-layer F0223. **a**, Crystal structure of F0223. We control the doping level of the sample by exposing it to a small air leak, which is known to introduce oxygen to the sample surface and dope hole carriers. **b, c**, FS mappings for the pristine and the surface-doped sample, respectively. **d**, MDC curves of the pristine and the surface-doped sample, taken along the colored line in **(b, c)**, respectively. Black lines are fits obtained by linear backgrounds and the Voigt functions (blue lines). **e, f**, Raw and symmetrized EDCs taken at various k_F points of the OP band in the pristine sample, respectively. The peaks indicated by orange arrows originate from the IP spectra. Colored squares indicate SC coherent peak positions. **g, h**, Raw and symmetrized EDCs taken at various k_F points of the IP band in the pristine sample, respectively. Colored circles indicate SC coherent peak positions. **i, j**, Similar to **(e, f)**, but for the surface-doped sample. **k, l**, Similar to **(g, h)**, but for the surface-doped sample. Colored arrows in **(g, k)** mark EDCs at the k_F points beyond the antiferromagnetic zone boundary (AFZB) marked by yellow shade in the inset of **(m)** toward the antinode. **m**, Summary of the IP and OP gap magnitudes in the pristine and surface-doped sample, plotted as a function of d -wave form. Colored lines represent fits to the data near the node and are used to extrapolate the SC gap magnitude at the antinode (Δ_0). The inset shows the determined Fermi surfaces and their fit to the tight-binding fit (colored lines). Errors of k_F is smaller than the symbol size.

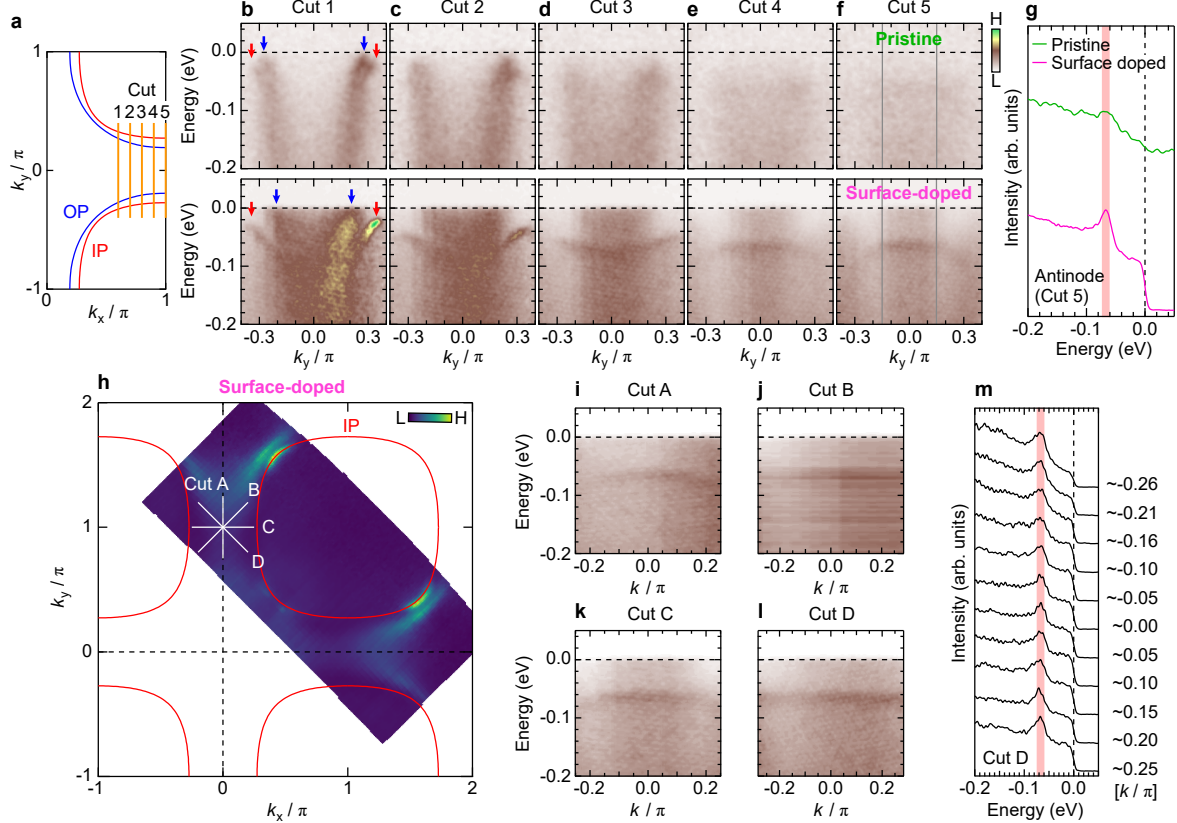


FIG. 5. Emergence of widely extended coherent flat band in the surface-doped three-layer F0223. **a**, Schematic FS of three-layered F0223. Orange lines indicate the momentum cuts used for **(b-f)**. **b-f**, Comparison of the band dispersions of the pristine (upper row) and the surface-doped (bottom row) sample, along the momentum cuts indicated in **(a)**. IP and OP bands are marked by red and blue arrows in **(b)**, respectively. **g**, Integrated EDCs of the pristine and the surface-doped F0223 at the antinode. The integrated momentum window is chosen to $[-0.15, +0.15]$ k_y/π (grey lines in **(f)**). Each curve is normalized by the energy window of $[-0.2, 0]$ eV. **h**, Fermi surface of the surface-doped F0223. Red line indicates a FS contour of IP estimated by the tight-binding method. **i-l**, ARPES band dispersions obtained from the momentum cut indicated in **(h)** (Cut A to D; white lines). **m**, EDCs, corresponding to panel **(l)**. Coherent peaks are marked by a red line, exhibiting a flat band.